Research Article Vol. 12, No. 4 / April 2024 / Photonics Research 701

PHOTONICS Research

Universal silicon ring resonator for error-free transmission links

JUNBO ZHU,[1,2,3] WEIWEI ZHANG,[1,*] KE LI,[1,4] BHARAT PANT,[1] MARTIN EBERT,[1] XINGZHAO YAN,[1] MEHDI BANAKAR,[1] DEHN T. TRAN,[1] CALLUM G. LITTLEJOHNS,[1] FUWAN GAN,[2] GRAHAM REED,[1] AND DAVID J. THOMSON[1,5]

[1]Optoelectronics Research Centre, University of Southampton, Southampton SO17 1BJ, UK
[2]National Key Laboratory of Materials for Integrated Circuits, Shanghai Institute of Microsystem and Information Technology, Chinese Academy of Sciences, Shanghai 200050, China
[3]University of Chinese Academy of Sciences, Beijing 100049, China
[4]Peng Cheng Laboratory, Shenzhen, China
[5]e-mail: d.thomson@soton.ac.uk
*Corresponding author: weiwei.zhang@soton.ac.uk

Received 13 October 2023; revised 5 December 2023; accepted 21 December 2023; posted 22 December 2023 (Doc. ID 509237); published 21 March 2024

We report the design, fabrication, and characterization of a universal silicon PN junction ring resonator for C band error-free communication links operated up to 50 Gb/s with co-designed optical modulation and detection performance. The universal p-n junction ring device shows co-designed detection responsivity up to 0.84 A/W, in conjunction with a modulation efficiency of $\sim$4 V · mm and >8 dB optical modulation extinction ratio, enabling C band 50 Gb/s NRZ communication link with a bit error rate $\leq 3 \times 10^{-12}$. Individually, the speed of modulation and detection is measured up to 112 Gb/s and 80 Gb/s, respectively. The principle of co-designing the PN junction ring modulator and detector performance required for error-free communication links can significantly ease the fabrication yield challenges of ring structures by reducing the number of types of devices. The principle can also be applied to O band wavelengths. To the best of our knowledge, for the first time, a device of this type has achieved both error-free modulation and detection operation up to 50 Gb/s in the C band individually or in conjugation as an error-free communication link, which paves the way to realize a >1.6 Tb/s all-silicon WDM-based error-free optical transceiver link in the future and is essential for future programmable photonics circuits.

Published by Chinese Laser Press under the terms of the Creative Commons Attribution 4.0 License. Further distribution of this work must maintain attribution to the author(s) and the published article's title, journal citation, and DOI.
https://doi.org/10.1364/PRJ.509237

1. INTRODUCTION

Over the past decades, the fast-growing bandwidth demand on data centers, artificial intelligence, clouding computing, and Internet of Things has driven the development of silicon photonics [1–3]. Benefiting from mature CMOS manufacturing techniques, silicon photonics integrated circuits have become a promising technology that aims to achieve system-level integration with low power consumption, low cost, small footprint, and high bandwidth. With no alteration to conventional CMOS materials and manufacturing processes, all-silicon optical transmission links have drawn a lot of attention [4].

As two indispensable building blocks of an all-silicon optical transceiver link, enormous efforts have been made to develop high-performance modulators (MODs) and photodetectors (PDs) individually [5–8]. However, the design differences required for PDs and MODs can significantly increase the complexity and the cost of fabrication as well as the electrical circuit design for wavelength control/trimming [9–15] and stabilization in the 300 mm silicon photonics platform [16–18]. Therefore, a universal structure with both high-speed modulation and detection operation will greatly enhance the silicon photonics integration level at low cost and can enrich programmable photonics circuits with more flexibility for light detection and modulation. Having one component that can function as either a modulator or a detector is attractive for a programmable circuit as it means the chip area that is required for would otherwise be needed for dedicated components to serve these functions that can be saved and/or the circuit that can be more versatile to serve a larger number of applications [19,20].

In the early stages, defect-mediated sub-bandgap absorption is observed in general carrier-depletion silicon modulators with

optical responsivity below 0.1 A/W and was proposed for optical power monitoring, for which data speed response at 35 Gb/s has been measured [21]. Silicon Mach–Zehnder interferometer (MZI)-type MODs and their straight PN-junction waveguide arm-based PDs have demonstrated error-free transmission links at a signal speed of 10 Gb/s for B2B and 10/20 km fibers [22,23]. Recently, owing to their compact size for co-packaged optics and resonance advantage for WDM links for high bandwidth optical I/O, micro-ring resonator (MR) devices have played a crucial role in the development of high bandwidth density Tb/s communication links. Unlike MZIs, the MR is a good candidate for co-designing optical modulation and detection properties via MR resonance enhancement (RE) effects. Early universal MR devices have shown 44 Gb/s modulation speed with a $V_\pi L$ of 1.7 V · cm [24] and 40 Gb/s detection speed with 48 mA/W responsivity under 8 V bias in the avalanche mode [25]. Photon-assisted tunneling (PAT) for sub-bandgap light detection in silicon PN-doped waveguides was later analyzed in the avalanche mode, where a strong electric field in the depletion region can generate the photon-assisted tunneling current due to impurity-assisted Franz–Keldysh absorption and amplify the generated photocurrent through avalanche multiplication gain, which is much less dependent on the defects in the doped silicon PN junction [26], enabling the MOD and avalanche photodetector (APD) to share the same PN junction and allowing a responsivity as high as 0.53 A/W to be measured in a ring resonator device [27]. In such case, O band 100 Gb/s PAM-4 can be measured with this responsivity benefiting from avalanche gain and a 3 dB OE bandwidth of ~25.5 GHz [27]. A modulation efficiency of $V_\pi L \sim 1$ V · cm and an EO bandwidth 40 GHz have also been achieved in the same device fabricated by using a standard foundry process [28]. A higher OE bandwidth of 35 GHz with a lower responsivity of 0.21 A/W and an EO bandwidth >50 GHz with $V_\pi L \sim 0.85$ V · cm have also been measured in another universal ring device with customized doping [29,30].

However, the performance of two previous universal MR devices either as a ring detector or modulator is limited and is inferior to the performance of state-of-the-art devices dedicated as either a modulator or detector. Currently, silicon ring PN junction MRs have been reported with impressive performance for individually optimized silicon MR-MODs and MR-PDs in the O band. For example, silicon ring modulators have reached an impressive high-speed operation of 128 Gbaud [31], while silicon ring detectors have been optimized up to 60 Gbaud (38 GHz) with a responsivity of 0.73 A/W [32]. A 4 × 50 Gb/s all-silicon ring-based WDM transceiver with CMOS ICs has demonstrated 50 Gb/s per wavelength error-free operation with a nonlinear feed-forward-equalizer (NL-FFE) enabled in the modulation side, and with a post-transimpedance amplifier (TIA) FFE and a decision-feedback-equalizer (DFE) enabled in the detection side by using an individually designed MR-APD and MR-MOD [4].

Now the question comes to specifically how we can achieve a high-performance universal ring device with state-of-the-art performances of the MR-APD and MR-MOD. Additionally, the PAT probability of sub-bandgap light absorption in the C band is weaker than absorption in the O band [26], which raises challenges in developing such a high-performance universal ring in the C band. So far, error-free communication links based on universal PN junction MRs have not been reported. These challenges are addressed here for the first time by co-designing the modulation efficiency of the MR-MOD to relax the MR-APD's bandwidth and noise for high-performance error-free optical links with low latency for cloud computing and networking in data centers.

In this work, we report a C band universal silicon PN junction MR with a resonance bandwidth from 1525 to 1565 nm, and designed to perform simultaneously as an APD and an MOD toward an error-free transmission link that is less dependent on the RF driver, TIA, and digital signal processor (DSP) chips. As an optical modulator a $V_\pi L$ of 4.0 V · mm and more than 8 dB modulation extinction ratio (ER) have been achieved with an RF driving voltage of $2.5V_{\mathrm{pp}}$. The photodetection performance shows a high responsivity up to 0.84 A/W before saturation and dark current <700 nA. The performance for both is comparable with the current state of the art as discussed above. The adopted co-design strategy for an error-free link relies on a large enough modulation ER to overcome its high noise-limited photodetection performance, achieving a bit error rate (BER) of 10^{-14} at 40 Gb/s without electrical and optical DSP or filters, and an BER of 3×10^{-12} (1×10^{-11}) at 50 (56) Gb/s with 3 taps FFE at the detection side. This work provides a universal C band silicon PN junction ring resonator design capable of performing as either an MR-APD or an MR-MOD, simplifying fabrication, and supporting error-free communication without DSP techniques for next-generation high-speed all-silicon optical transmission applications.

2. DESIGN

The schematic diagram of the optical transmission link is shown in Fig. 1. The performance of the modulator and detector needs to be co-designed to realize error-free data transmission enabled by the universal MR. Typically, the BER is estimated by $0.5 \cdot \mathrm{erfc}(Q/\sqrt{2})$ and $\mathrm{erfc}(\cdot)$ is the complementary error function. Q can be defined as Eq. (1), where μ_1 and μ_0 represent the high and low voltage levels of the signal; σ_1 and σ_0 are Gaussian approximations of the receiver noise, respectively; $\mathcal{R}$ is the responsivity of the MR detector; P_{AVG} is the average of the received optical power $(P_1 + P_0)/2$; P_1 and P_0 represent the high and low power levels of the modulated optical signal; ER represents the extinction ratio of the modulated optical signal; and $Z_{\mathrm{TIA}}(\omega)$ represents the TIA function converting current levels to voltage levels:

$$Q = \frac{|\mu_1 - \mu_0|}{\sigma_1 + \sigma_0} \sim P_{\mathrm{AVG}} \frac{\mathrm{ER} - 1}{\mathrm{ER} + 1} \mathcal{R}(\omega) \frac{Z_{\mathrm{TIA}}(\omega)}{\sigma_1 + \sigma_0}. \tag{1}$$

Under the approximation of Eq. (1) and given the total noise $(\sigma_1 + \sigma_0)$, the BER performance of an MR-MOD- and MR-APD-based communication link is mainly determined by (1) the input optical power P_{AVG} and the ER of the modulated optical signal, and (2) the responsivity $\mathcal{R}$ of the MR-APD. The noise from the MR-MOD and MR-APD is also expected to be low enough for TIA circuits to handle the final error-free

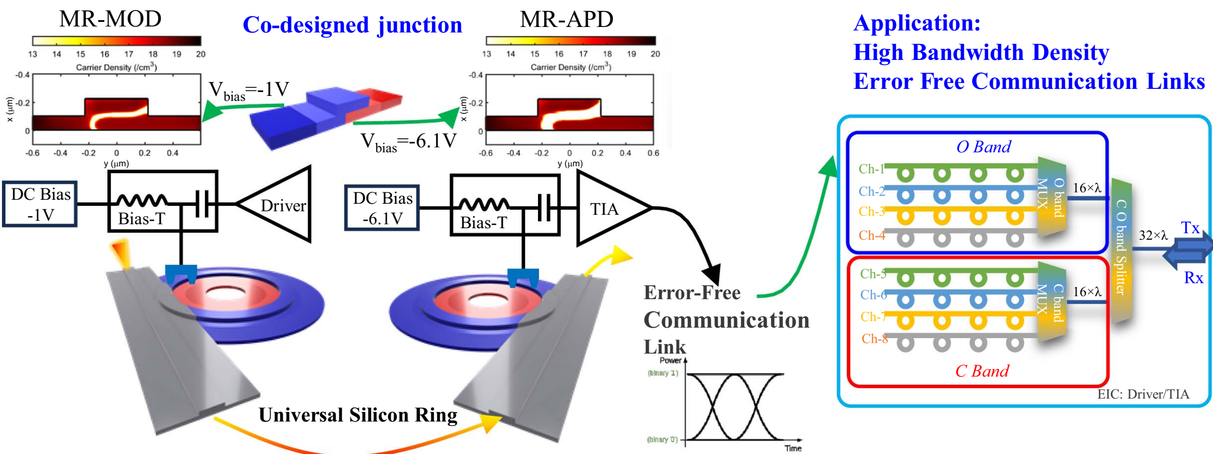

Fig. 1. Schematic diagram of an error-free transmission link enabled by a universal MR, and its application to scale up for 32λ in O and C band for a 1.6 Tb/s error free link (Appendix C).

operation. In this work, the TIA design for low-noise operation is not discussed and the main focus is to develop a high-performance universal silicon PN junction MR for robust error-free communication that is less dependent on signal processing enabled by DSP, TIA, and other electrical or optical filters, etc. Consequently, the optoelectronics properties of the universal ring device as MR-MOD and MR-APD are co-designed to both achieve a high modulation ER at given P_{AVG} for the MR-MOD and a high $\mathcal{R}$ for the MR-APD. For a given P_{AVG} and laser power P_{in}, the average optical power insertion loss (IL_{AVG}) of the MR-MOD is defined as $\text{IL}_{\text{AVG}} = -10 \log 10(P_{\text{AVG}}/P_{\text{in}})$. Therefore, a lower IL_{AVG} is better. The modulated optical signal after the MR-MOD should be error free before being detected by the MR-APD. When the optical signal is converted into an electrical signal by the MR-APD and TIA, the detected signal's BER will be also affected by the received power P_{AVG}, responsivity $\mathcal{R}$, and dark current of the MR-APD.

As a universal ring device for MOD and APD, the co-design is focused on a range of performance metrics: modulation efficiency $V_\pi L$, responsivity $\mathcal{R}$, dark current I_{dark}, and IL_{AVG}. To engineer these performances, we adopted an L-shape PN junction in a silicon rib waveguide, as shown in Figs. 1 and 2(c), which has a larger overlap area between the depletion region and optical mode than the conventional lateral PN junction, resulting in better modulation and detection efficiency. The universal ring design is based on a 10 μm radius micro-ring structure with an active doping region around 73% of its circumference. The waveguide dimensions are 450 nm × 220 nm with a 100 nm high slab.

A larger Q-factor can result in better responsivity via the resonance enhancement effect, but also limits the optical bandwidth with longer photon lifetime. Here we design the optical 3 dB bandwidth (f_{FWHM}) close to 50 GHz to support error-free high-speed modulation and detection at 50 Gbaud, which means the Q-factor should be close to or lower than 3800 for resonant wavelengths (λ_{res}) around 1550 nm by Eq. (2). Under critical coupling, α and r both are about 0.94 to meet the Q-factor value of 3800. The optical waveguide loss (α_L) is approximately 12 dB/mm:

$$Q = \frac{\lambda_{\text{res}}}{\text{FWHM}} = \frac{f}{f_{\text{FWHM}}} = \frac{\pi\sqrt{r\alpha}Ln_g}{\lambda_{\text{res}}(1 - r\alpha)}. \quad \textbf{(2)}$$

The universal MR with L-shape PN junction, as shown in Fig. 1, is also designed to operate with an electrical bandwidth of 50 GHz as typically required for high signal integrity operation and 50 Gbaud error-free data transmission. By the lumped bandwidth model of Eq. (3), the ring junction capacitance (C_L) has an upper limit value of about 64 fF when only considering the 50 Ω source impedance (R_S). Considering 73% region of the designed MR is doped as an active PN junction, the capacitance per length limit of the PN junction cross section (C_{PN}) is 1.4 fF/μm:

$$\text{BW}_E = \frac{1}{2\pi(R_S + R_L)C_L}. \quad \textbf{(3)}$$

The doping profile of the PN junction was optimized to achieve high modulation and detection efficiency with the constraints of the discussed parameters, 12 dB/mm optical waveguide loss α_L, and 1.4 fF/mm PN junction capacitance C_{PN}. The modulation and detection, relying on the plasma dispersion effect [33] and the PAT effect [26], both occur in the depletion region, the width of which is given by

$$w = \sqrt{\frac{2\varepsilon}{q} \cdot \frac{N_A + N_D}{N_A N_D} \cdot \Delta V}, \quad \textbf{(4)}$$

where ε is the dielectric permittivity of silicon, q is the electron charge, and $N_{A/D}$ is the p- and n-type doping concentrations. ΔV is the difference between the built-in voltage and bias voltage. The width of the depletion region is proportional to the square root of the doping concentration $\sqrt{N_{A/D}}$, as shown by Eq. (4). The effective absorption coefficient of PAT ($\Gamma \cdot \alpha_t$) is related to the confinement/overlap factor (Γ) of the optical mode in the depletion region. α_t is the PAT absorption coefficient. A larger doping concentration provides more carriers for modulation and therefore increasing the doping level provides

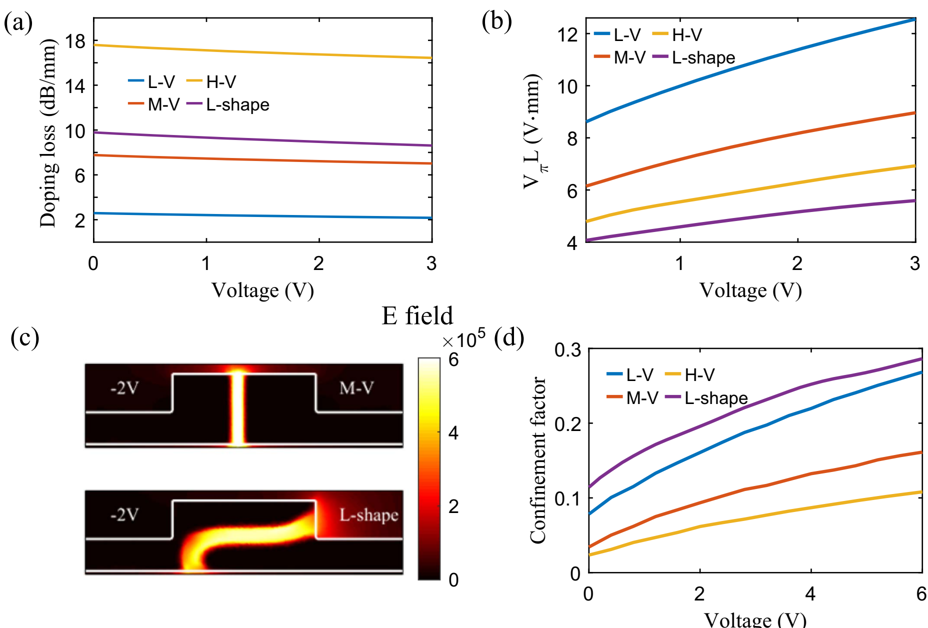

Fig. 2. Simulated (a) doping losses, (b) modulation efficiencies, (c) electric field density distribution, and (d) confinement factors of the low doping vertical junction (L-V), medium doping vertical junction (M-V), high doping vertical junction (H-V), and medium doping L-shape junction (L-shape) produced by using Silvaco TCAD and Lumerical.

an enhancement of the modulation efficiency, but will decrease the width of the depletion region, which results in a reduction of the photon absorption efficiency.

To find a good trade-off between $V_\pi L$ and photon absorption efficiency under all of the above restrictions, the PN junction is designed, with simulated key parameters α_L (8–10 dB/mm), Γ (0.12–0.29), and $V_\pi L$ (4–5.8 V · mm), as shown in Fig. 2. We also compared the simulated parameters (α_L, Γ, $V_\pi L$) of the proposed device (medium doping $\sim 2.5 \times 10^{18}$ cm^{-3}, L-shape) with devices having vertical PN junctions at different doping levels: lower doping ($\sim 1 \times 10^{18}$ cm^{-3}, L-V), medium doping ($\sim 2.5 \times 10^{18}$ cm^{-3}, M-V), and higher doping ($\sim 5 \times 10^{18}$ cm^{-3}, H-V). The p-type region of the vertical PN junction is optimized to be 20 nm wider than the n-type region, because free holes have a smaller absorption and a larger shift of the real part of the refractive index than free electrons in silicon.

As shown in Fig. 2(c), the L-shape structure has an ∼2 times wider depletion area while it still keeps a narrow depletion width (w), which is important for high-speed detection and modulation. From Figs. 2(a) and 2(b), the L-shape structure exhibits excellent $V_\pi L$ performance with resonable doping loss. The L-shape PN junction also shows a better spatial overlap between the depletion region and the optical mode profile, as shown in Fig. 2(d), which will significantly enhance the total photon absorption efficiency via PAT. These results suggest that the proposed universal ring resonator with an L-shape PN junction possesses excellent performance in terms of modulation and detection.

3. DC CHARACTERIZATION

The device fabrication is summarized in Appendix A, and the radius is 10 μm. The measured transmission spectrum is shown in Fig. 3(a), in which the Q-factor is about 4200, the DC ERs are ∼30 dB, and the free spectral range (FSR) is ∼10 nm. The fabricated devices show high insertion losses from grating to grating, about 20 dB, caused by modifications to the standard foundry process flow inducing extra grating losses. This can be rectified in the future by using a different grating coupler

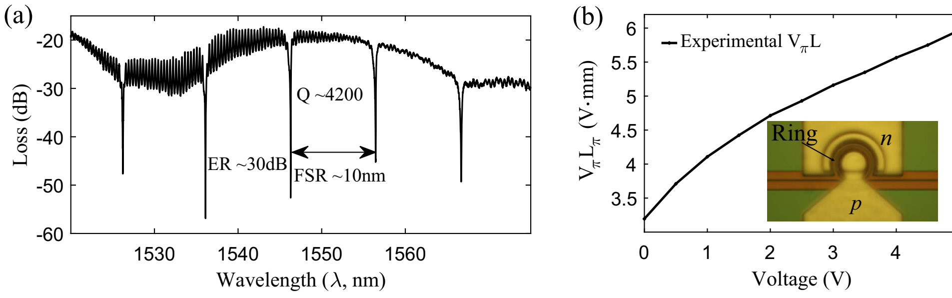

Fig. 3. Measured (a) transmission spectrum and (b) phase change efficiency of 10 μm radius MR.

design. The parameters of the ring resonator are then extracted. The self-coupling coefficient (r) and round-trip optical ring resonator attenuation (α) are extracted as ~0.94. Thus, the corresponding cavity resonance enhancement RE [34] is calculated as ~9. The measured phase shift efficiency of the micro-ring is shown in Fig. 3(b), which shows a good agreement with simulation results.

The measured MR-MOD resonance shifts with applied bias are shown in Fig. 4(a). With a $2.5V_{pp}$ swing, a large DC ER of 14 dB can be achieved with a one level IL of about 4 dB, as shown in Fig. 4(b). The PAT probability is expressed as [26,35]

$$T \approx \exp\left(-\frac{4\sqrt{2m_e^*}}{3\hbar}\sqrt{E_b}w_b\right), \tag{5}$$

where m_e^* is the electron's effective mass in silicon, E_b is the potential barrier height, and w_b is the effective barrier width. The simulated electrical field of the Si L-shape PN junction at 0 and −6.1 V is shown in Fig. 4(c). By increasing the reverse bias voltage, the electrical field becomes stronger and the depletion width (w) becomes larger, which increases the PAT effective absorption coefficient with larger overlap between the optical mode and depletion region, also as shown in Fig. 4(c). From the simulated energy bandgap in Fig. 4(c), w_b decreases from ~8.2 nm at 0 V to ~2.1 nm at −6.1 V. The reduced w_b can increase the tunneling probability exponentially by Eq. (5). In addition, the maximum electrical field ($>1 \times 10^6$ V/cm) at −6.1 V is sufficient to trigger impact ionization in silicon for avalanche gain. Therefore, the measured responsivity at the resonant wavelength [Fig. 4(d)] exhibits an exponential-like increase at high reverse bias voltages due to the exponential increase of PAT absorption and avalanche gain. With the help of resonant enhancement, 0.84 A/W responsivity has been measured when the bias voltage is −6.1 V and the input optical power is −10.5 dBm before reaching saturation.

While working as an APD, the measured dark current and total current of the MR-APD with different input optical powers are shown in Fig. 5(a). The dark current is about 700 nA at −6.1 V. As shown in Figs. 5(b) and 5(c), the responsivity decreases with injected optical power, which can be attributed to avalanche gain saturation in APDs [36]. From Fig. 5(d), we can see that even though the responsivity decreases with optical power, the current at high voltages still increases significantly, showing a high photocurrent of 0.3 mA with around 5.1 dBm of input optical power at −6.1 V.

4. RF CHARACTERIZATION

The bandwidth of the depletion ring is first estimated by high-speed data transmission experiments. 80 Gb/s optical modulation eye diagrams (without pattern averaging) and 50 Gb/s optical detection eye diagrams (without pattern averaging) have been measured to determine whether their bandwidths are above 35 GHz (Appendix B). To be noted, when operating as an MR-APD, the eye diagram is limited by intrinsic noise and the performance of a 40 GHz lithium niobate MZI modulator (LN MZI-MOD) used to generate the high-speed optical signal, for which the 80 Gb/s optical eye-diagram is closed (Appendix B) and therefore extra FFE taps are needed for the MR-APD measurement. The detailed test setup and testing process are summarized in Appendix B.

High-performance detection by an MR-APD with a BER level around 10^{-12} has been achieved at lower data rates without the help of using dedicated low-noise TIAs and electrical and optical filters in the detection side. The measured 40 Gb/s, 50 Gb/s, and 56 Gb/s eye diagrams of the MR-APD with input

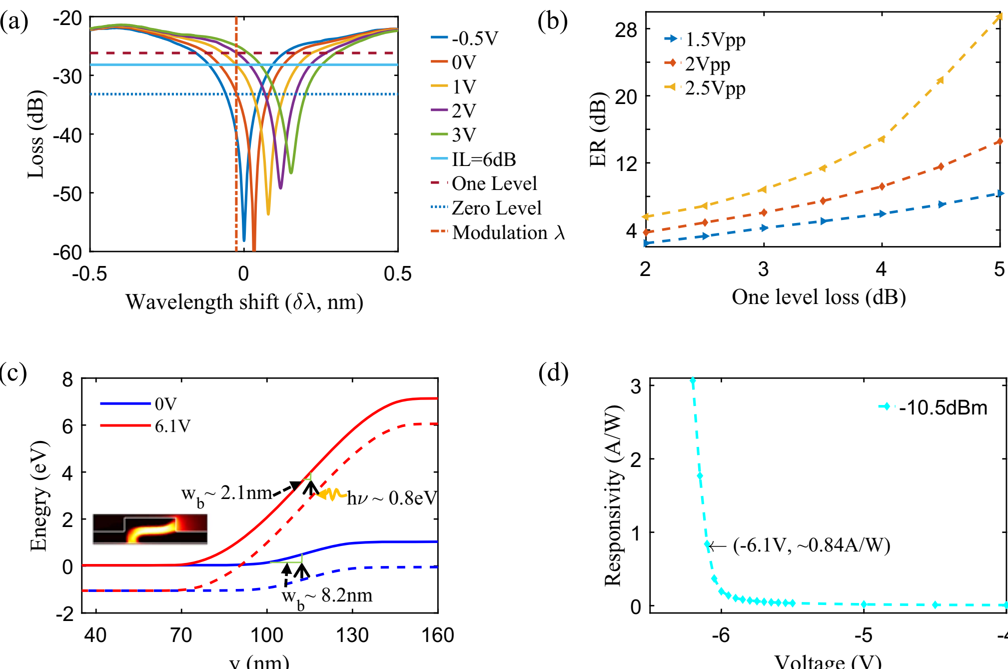

Fig. 4. Measured (a) DC electro-optical wavelength shifts and (b) DC ER versus one level losses with different voltage swings. (c) Simulated conduction and valence band diagrams of the Si L-shape PN junction at different bias voltages. (d) Measured responsivity versus bias voltage.

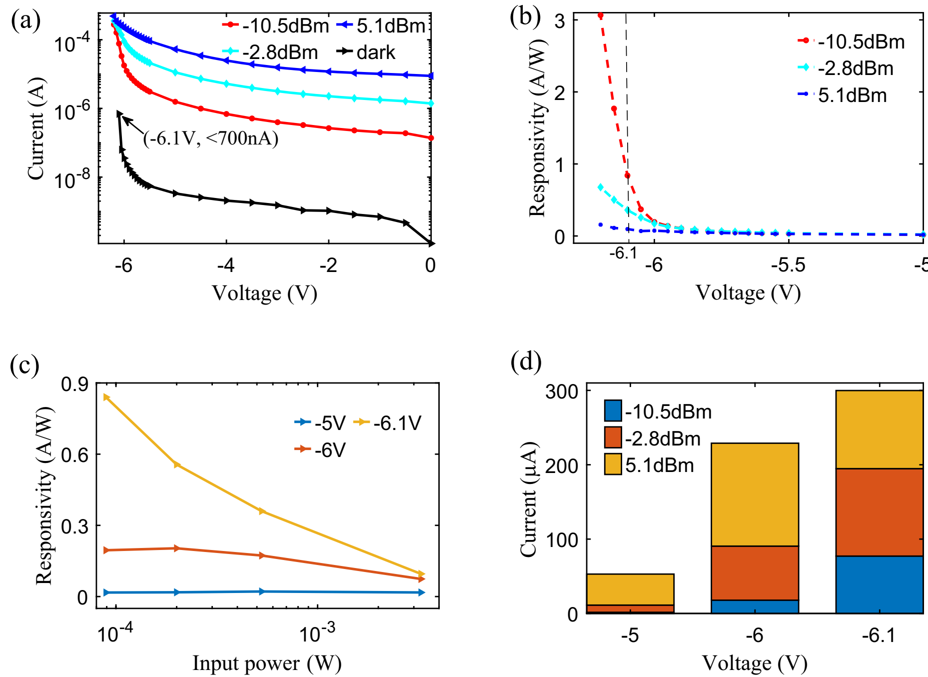

Fig. 5. Measured (a) dark and total current versus bias voltage for different optical input powers, (b) responsivity versus bias voltage at different input optical powers, (c) responsivity versus input optical power at different bias voltages, (d) total current at different voltages and optical input powers.

bus waveguide optical power of ~6 dBm at 6.1 V bias are shown in Figs. 6(a)–6(c). BERs of 8×10^{-13} at 40 Gb/s (without FFE), 3×10^{-12} at 50 Gb/s (3 taps FFE), and 1×10^{-11} at 56 Gb/s (3 taps FFE) are measured. To reach a BER of 8×10^{-13} or even lower at 40 Gb/s, the required optical power from the transmitter (Tx) (average power of the modulated signal from the LN MZI-MOD) is 6 dBm and the required optical modulation ER is about 7.1 dB. Despite the dark current of ~700 nA and excess noise of Si, the receiver (Rx) side has also tolerated the amplified spontaneous emission noise from the erbium-doped fiber amplifier (EDFA) (with no optical filters) required due to the high IL of the grating couplers. And neither noise filter was enabled in the electrical port of the digital communication analyzer. In addition, a linear amplifier was used instead of a TIA for the Rx. Therefore, the optical sensitivity of the Rx can be further improved in future work by overcoming high grating losses and integration with dedicated electrical Rx circuits (TIA, filter, etc.).

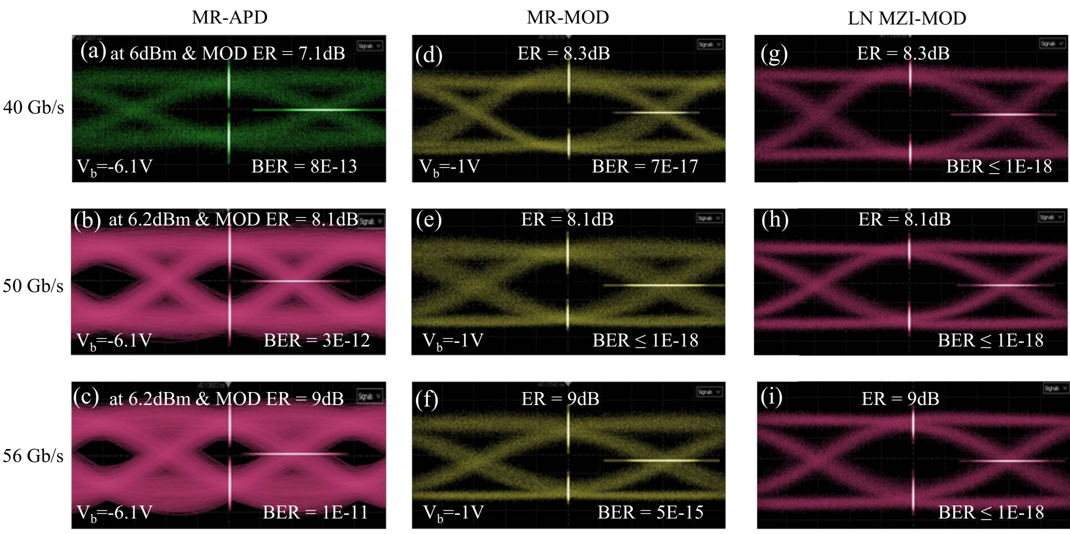

Fig. 6. Measured eye diagrams of MR-APD at bit rates of (a) 40 Gb/s, $P_{in} = 6$ dBm, and MOD ER = 7.1 dB; (b) 50 Gb/s, $P_{in} = 6.2$ dBm, and MOD ER = 8.1 dB, with 3 taps FFE; (c) 56 Gb/s, $P_{in} = 6.2$ dBm, and MOD ER = 9 dB, with 3 taps FFE. Eye diagrams of MR-MOD at bit rates of (d) 40 Gb/s, ER = 8.3 dB; (e) 50 Gb/s, ER = 8.1 dB; (f) 56 Gb/s, ER = 9 dB. Eye diagrams of LN MZI-MOD at bit rates of (g) 40 Gb/s, ER = 8.3 dB; (h) 50 Gb/s, ER = 8.1 dB; (i) 56 Gb/s, ER = 9 dB.

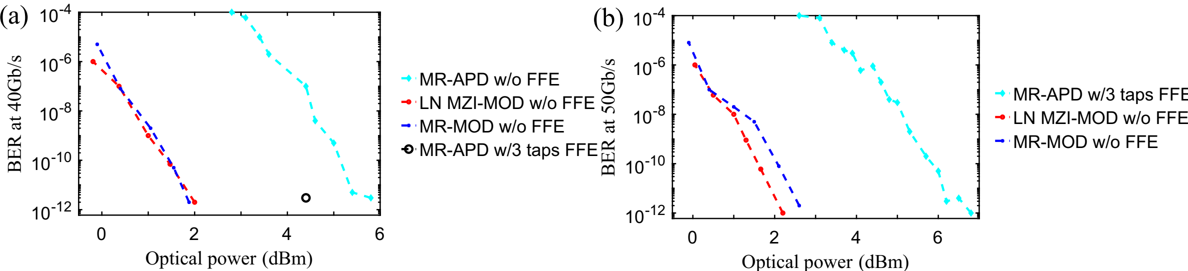

Fig. 7. Measured (a) 40 Gb/s and (b) 50 Gb/s NRZ BER with different optical power for the MR-APD, MR-MOD, and LN MZI-MOD.

For comparison, by sending the same modulated optical signal from the LN MZI-MOD to the reference PD of the 65 GHz optical detector within the Keysight 86116C-40 (with noise filter off, the sensitivity is −5 dBm and when the filter turned on at 40 Gb/s, the characteristic RMS noise is 36 μW), the required optical power is about 2 dBm to reach a BER level of $\sim 1 \times 10^{-12}$, as shown in Fig. 7. Under the same conditions, to reach a BER of $\sim 1 \times 10^{-12}$ at 50 Gb/s, the required optical power in the bus waveguide of the MR-APD is about 6.2 dBm. The BER performance of the MR-MOD is also compared with the LN-MZI-MOD in Fig. 7. At 40 Gb/s and 50 Gb/s, the measured optical power VS BER is similar, and both can reach high optical ER > 8 dB and very low BER $< 5 \times 10^{-15}$ for data rates 40–56 Gb/s. The MR-MOD is biased at −1 V and driven with an RF voltage of $\sim 2.5 V_{pp}$. At 40 Gb/s, the BER for MR-APD reaches the order of 10^{-12} when the received optical power is 6 dBm and the input ER is 7 dB. The optical power can be reduced to 4.4 dBm when 3 taps FFE is enabled. At 50 Gb/s, the BER of the MR-APD is of the order of 10^{-12} with 3 taps FFE enabled and 7 dBm optical power.

5. DISCUSSION

When the bit rate exceeds 40 Gb/s, the BER performance of the MR-APD is mainly limited by the degraded modulated optical signal of the LN MZI-MOD. As illustrated in Fig. 8, the SNR of the modulated optical signal generated by the LN MZI-MOD quickly rolls off from 10 to 5 when the bit rate increases from 40 Gb/s to 64 Gb/s, which is the fundamental bottleneck for this work to demonstrate error-free detection beyond 50 Gb/s. We have also measured comparable SNR (in Fig. 8) and ER/BER (in Fig. 6) performance of the MR-MOD in comparison with the LN MZI-MOD. The IL_{AVG} of the high ER eye diagrams measured in Fig. 6 can be reduced to as low as 6 dB. These

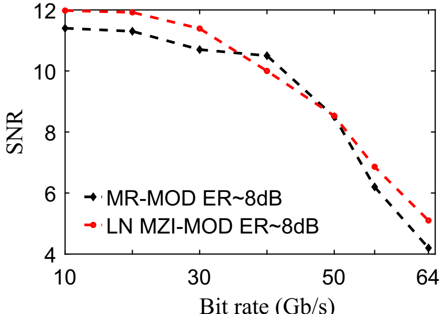

Fig. 8. Measured SNR of the MR-MOD and LN MZI-MOD at different bit rates with the same ER of 8 dB.

results demonstrate that the MR-MOD can produce high-quality modulated optical signals comparable to those generated by the LN MZI-MOD for supporting the error-free detection.

Finally, we show the impact of co-designing the MR-APD and MR-MOD on the BER performance of the Rx. As shown in Figs. 9(a)–9(c), the measured BER of the Rx at a data rate of 40 Gb/s is strongly dependent on the Tx ER. The BER significantly decreases from 10^{-6} to 10^{-14} when the ER increases from 4 dB to 8.2 dB and the received optical power is kept at 6 dBm. Such a high ER performance has been co-designed and achieved for the MR-MOD as shown in Fig. 6. Based on the performance analysis of the MR-APD and the MR-MOD (6 dB IL_{AVG}), an error-free communication link can be built by simply using the co-designed universal depletion ring resonator with coupled optical power of about 12 dBm.

In Table 1, we summarize the measured performance and compare with state-of-the-art reports of CMOS-SiPh transceiver demonstrations. Despite not being integrated with a CMOS TIA and driver, our presented results clearly stand out in terms of both modulation and detection performance (Table 2) as well as higher-speed error-free operation with less overhead coding for forward-error correction. This can reduce the requirement for electronic devices to reconstruct the original bit stream and facilitate large-scale integration with low power consumption and lower latency. The current unpackaged approach suffers for optical noise from the EDFA, and the sensitivity of the Keysight 86116C-40 (with noise filter off) increases to 2 dBm from −5 dBm when the noise filter turned on at 40 Gb/s, which means there is a potential for 7 dB of laser power reduction if the MR-APD-based Rx performances are compared with the Rx of the Keysight 86116C-40. Current state-of-the-art TIA design based on 16 nm FinFET technology only requires 80 μA (peak-peak) current amplitude for error-free operation when integrated with a GeSi waveguide PD [39]. For our co-designed MR-APD, it shows a current amplitude of 110 μA (peak-peak) when the input optical power is switched from −10.5 dBm to −2.8 dBm, as shown in Fig. 5(d). Therefore, it is possible to realize a low-sensitivity MR-APD Rx at about −6.5 dBm with the help of a dedicated TIA and further optimization of the Si APD, and the optical power budget of the laser can be reduced to less than 0 dBm when only considering the insertion loss from the MR-MOD, which is about 12 dB lower than the current unpackaged demonstration where the Rx side utilized a linear RF amplifier. All passive integration should also be improved with negligible insertion loss. Beyond the optical co-design approach explained in this work, co-design of the Tx and Rx electronics circuits can

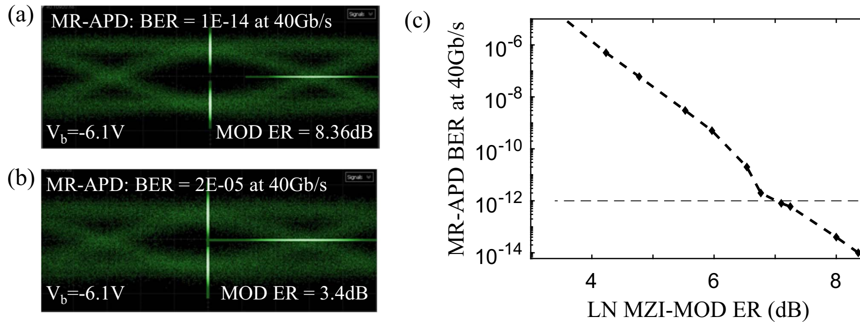

Fig. 9. Measured eye diagrams of the MR-APD at 40 Gb/s and $P_{\text{in}} = 6$ dBm with (a) MOD ER = 8.36 dB and (b) MOD ER = 3.4 dB; (c) 40 Gb/s NRZ BER of the MR-APD decreases with an increasing modulated optical ER of the LN MZI-MOD.

Table 1. Performance Summary and Comparison between State-of-the-Art Ring-Based CMOS Optical Links and Our Work

	[37]-2012	[38]-2019	[39]-2020	[4]-2021	[40]-2023	This Work
Integration	130 nm SOI driver, TIA	14 nm FinFET driver, TIA	16 nm FinFET driver, TIA	28 nm CMOS driver, TIA	CMOS driver, TIA	Unpackaged
Laser power	7.6 dBm	>8 dBm	/	6 dBm	8.1 dBm	12 dBm
Wavelength	C band	O band	C band	O band	O band	C band
Tx MOD	Ring	Ring	GeSi EAM	Ring	Ring	Ring
Tx driver	2 V	1.4 V	1.8 V	2.6 V	1.3 V	2.5 V
Tx BER	1×10^{-12} 25 Gb/s w/pre-emphasis	OMA = −10 dBm 40 Gb/s	$<1 \times 10^{-12}$ 50 Gb/s w/pre-equalization	$<1 \times 10^{-12}$ 50 Gb/s	$<1 \times 10^{-12}$ 40 Gb/s	1×10^{-15} 56 Gb/s
Tx ER	6.9 dB	4.6 dB	>3 dB	4.3 dB	5.3 dB	>8 dB
Rx PD	Ge PD	Ge PD	GeSi PD	Si ring PD	Ge PD	Si ring PD
PD responsivity	0.8 A/W	1 A/W	1 A/W	0.23 A/W	0.94 A/W	0.84 A/W
Rx BER	10^{-12} 25 Gb/s	$<1 \times 10^{-12}$ 38 Gb/s	$<1 \times 10^{-12}$ 50 Gb/s w/CTLE	$<1 \times 10^{-12}$ 50 Gb/s FFE + DFE	$<1 \times 10^{-12}$ 40 Gb/s	1×10^{-14} 40 Gb/s 3×10^{-12} 50 Gb/s with 3 taps FFE

Table 2. Performance Summary and Comparison between State-of-the-Art Universal Devices and Our Work

Type	Responsivity (A/W)	$V_\pi L$ (V · cm)	Bandwidth (GHz)
Si-ring [21]	5.9×10^{-3}	/	~12
Si-ring [24,25]	48×10^{-3}	1.7	20
Si-MZI [22,23]	0.54	0.81	26
Si-ring [27,28]	0.53	1	25.5
Si-ring [29]	0.21	0.825	35
Our work	0.84	0.4	>35

also further reduce the link power budget toward higher-speed operation with lower power consumption in the future.

6. CONCLUSION

In this work, we have demonstrated a silicon depletion universal ring with co-designed high-performance properties of optical modulation (4 V · mm) and optical detection ($\mathcal{R}$ 0.84 A/W), allowing error-free communication links operating up to 50 Gb/s. Based on our current demonstrated results, the MR-APD needs around 6 dBm (4 mW) input optical power and an optical ER of 7 dB to generate OE conversion with a BER $< 1 \times 10^{-12}$, indicating that the link requires a coupled laser power ≥12 dBm (16 mW) in consideration of 6 dB IL_{AVG} due to the MR-MOD. The co-designed MR-MOD can fulfill this high optical power operation with low BER $< 5 \times 10^{-15}$ and high modulation ER > 8 dB. In the future, integration with a CMOS driver with better signal integrity and SNR for the MR-MOD Tx and also with dedicated low-noise TIA circuits for the MR-APD will significantly improve the BER of the transmission link [4] beyond 50 Gb/s. Our work proves the principle of using a universal ring device to form a high-speed error-free communication link in the optical C band, which can be also applied to the O band and thus provides a simplified all-silicon universal ring resonator solution for WDM-based error-free communication links beyond 1.6 Tb/s (see Appendix C) in the future and for programmable photonics circuits configured for multi-function purpose.

APPENDIX A: FABRICATION

The fabrication of the silicon depletion ring resonators is based on 8-inch (1 inch = 2.54 cm) SOI wafers by using the open-source, license-free silicon photonics prototyping foundry

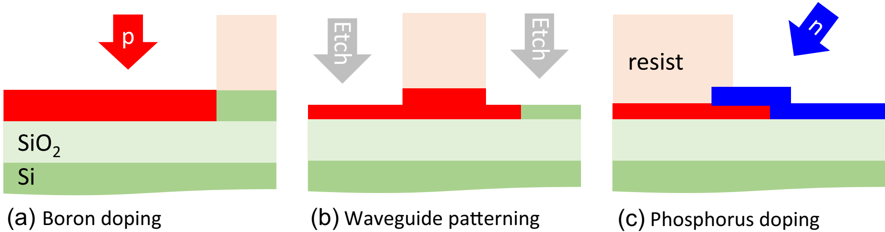

Fig. 10. (a)–(c) Schematic diagrams of doping micro-ring to form L-shape PN junctions with 6 rotations.

CORNERSTONE [41]. The fabrication process flow can be found in Ref. [41], and the doping process to form the L-shape PN junction is customized. In the fabrication process, boron is initially doped into the 220 nm thick silicon active region, and then the waveguide is etched. Afterwards, phosphorus doping is carried out with a tilt angle of 45 deg and six equal rotations between 0 and 360 deg to form the L-shape doping profiles all around the resonators, as depicted in Fig. 10. The n+ and p+ targeted at a doping level of $\sim 1 \times 10^{20}$ cm^{-3} were added layer.

APPENDIX B: EYE DIAGRAM MEASUREMENTS

For the performance measurement of the MR-APD, CW laser light first went through a polarization controller (PC), and then

Fig. 11. Experimental setup for eye diagram and BER measurements of (a) MR-APD and (b) MR-MOD.

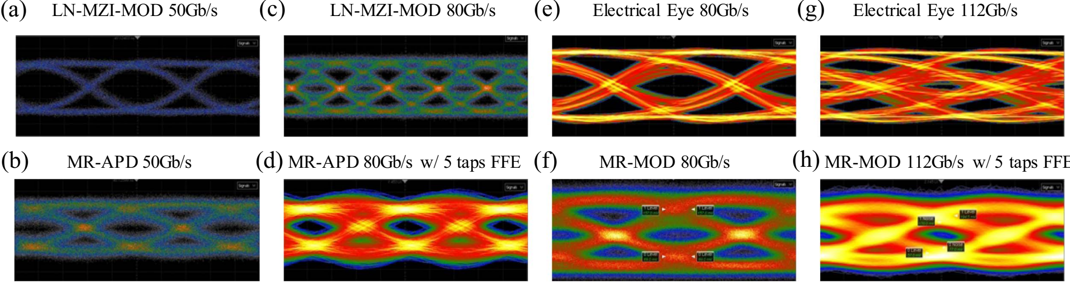

Fig. 12. Measured eye diagrams of (a) LN-MZI-MOD at 50 Gb/s, (b) MR-APD at 50 Gb/s, (c) LN-MZI-MOD at 80 Gb/s, (d) MR-APD at 80 Gb/s with 5 taps FFE and eye average, (e) RF signal before the RF probe at 80 Gb/s, (f) MR-MOD at 80 Gb/s, (g) RF signal at 112 Gb/s, (h) MR-MOD at 112 Gb/s with 5 taps FFE in the DCA.

was modulated by a 40 Gb/s LN MZI-MOD. The modulated optical signal was then amplified with a two-stage EDFA before it was coupled to the MR-APD through a second PC. The photocurrent signal was then collected by a combination of a 67 GHz RF open probe, a 64 GHz bias tee, and a 60 GHz RF linear amplifier, and then sent to the 80 GHz electrical port of a Keysight digital communication analyzer (DCA-X 86100D + Agilent 86116C-040), as shown in Appendix B, Fig. 11(a). The BER characterization is done in jitter mode. The eye diagrams and BER characterization of the LN-MZM and MR-MOD were detected by the 65 GHz optical detector of the Keysight DCA with the SIRC and filter off, as shown in Appendix B, Fig. 11(b). Two PRBS11 data are generated and sent to the MUX. The measured eye diagrams of LN-MZI-MOD, MR-APD, MR-MOD, and RF signal are shown in Fig. 12.

APPENDIX C: WAVELENGTH-DIVISION (DE) MULTIPLEXING FOR 1.6 Tb/s

The envisioned 1.6 Tb/s Tx or Rx can be achieved by using four FSR windows of MR-APD/MOD in the O and C bands, as shown in Fig. 13, which means four wavelengths are operating in one FSR range about 10 nm, which is large enough for supporting error-free operations [4]. The passive (de)multiplexing used for dividing wide band into four wavelength windows with 10 nm separation can be achieved with low loss <1 dB [42]. And the demonstrated passive (de)multiplexing for the O/C band also shows low insertion loss (<1 dB) and high extinction ratio (>20 dB) [43]. These settings of 1.6 Tb/s ring arrays guarantee fully utilizing the lasers, modulators, and detectors developed for O/C bands, and cross talk between different rings and wavelength bands is largely suppressed. Therefore, error-free operation is possible to achieve in the future.

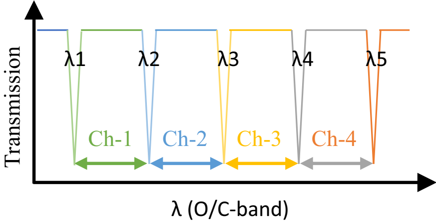

Fig. 13. MR's four FSR channels have to be matched with MUX/De-MUX channels. Four MRs operate in each channel, and 16 in total for the C and O band.

Funding. National Key R & D Program of China (2022YFB2803100); Engineering and Physical Sciences Research Council (EP/N013247/1, EP/T019697/1, EP/W035995/1); National Major Scientific Research Instrument Development Project (22127901); Shanghai Sailing Program (22YF1456700); China Scholarship Council (CSC); Royal Society (UF150325).

Acknowledgment. D. J. Thomson acknowledges funding from the Royal Society for his University Research Fellowship.

Disclosures. The authors declare no conflicts of interest.

Data Availability. All data supporting this study are available upon request from the University of Southampton repository at [44].

REFERENCES

1. D. J. Thomson, A. Zilkie, J. E. Bowers, *et al.*, "Roadmap on silicon photonics," J. Opt. **18**, 073003 (2016).
2. H. Wu and Q. Dai, "Artificial intelligence accelerated by light," Nature **589**, 25–26 (2021).
3. W. Gropp, S. Banerjee, and I. Foster, "Infrastructure for artificial intelligence, quantum and high performance computing," arXiv, arXiv:2012.09303 (2020).
4. H. Li, Z. Xuan, R. Kumar, *et al.*, "A 4 × 50 Gb/s all-silicon ring-based WDM transceiver with CMOS IC," in *European Conference on Optical Communication (ECOC)*, pp. 1–3.
5. W. Zhang, M. Ebert, K. Li, *et al.*, "Harnessing plasma absorption in silicon MOS ring modulators," Nat. Photonics **17**, 273–279 (2023).
6. Y. Peng, Y. Yuan, W. V. Sorin, *et al.*, "All-silicon microring avalanche photodiodes with a >65 A/W response," Opt. Lett. **48**, 1315–1318 (2023).
7. M. Sakib, P. Liao, R. Kumar, *et al.*, "A 112 Gb/s all-silicon micro-ring photodetector for datacom applications," in *Optical Fiber Communications Conference and Exhibition (OFC)*, pp. 1–3.
8. G. T. Reed, G. Mashanovich, F. Y. Gardes, *et al.*, "Silicon optical modulators," Nat. Photonics **4**, 518–526 (2010).
9. B. Chen, X. Yu, X. Chen, *et al.*, "Real-time monitoring and gradient feedback enable accurate trimming of ion-implanted silicon photonic devices," Opt. Express **26**, 24953–24963 (2018).
10. X. Yu, X. Chen, M. M. Milosevic, *et al.*, "Electrically erasable optical I/O for wafer scale 268 testing of silicon photonic integrated circuits," IEEE Photonics J. **12**, 3027799 (2020).

11. X. Yu, X. Chen, M. M. Milosevic, *et al.*, “Ge ion implanted photonic devices and annealing for emerging applications,” Micromachines **13**, 291 (2022).
12. R. Loiacono, G. T. Reed, G. Z. Mashanovich, *et al.*, “Laser erasable implanted gratings for integrated silicon photonics,” Opt. Express **19**, 10728–10734 (2011).
13. H. Li, G. Balamurugan, T. Kim, *et al.*, “A 3-D-integrated silicon photonic microring-based 112-Gb/s PAM-4 transmitter with nonlinear equalization and thermal control,” IEEE J. Solid-State Circuits **56**, 19–29 (2020).
14. N. Mehta, S. Lin, B. Yin, *et al.*, “A laser-forwarded coherent transceiver in 45-nm SOI CMOS using monolithic microring resonators,” IEEE J. Solid-State Circuits **55**, 1096–1107 (2020).
15. S. Agarwal, M. Ingels, M. Pantouvaki, *et al.*, “Wavelength locking of a Si ring modulator using an integrated drop-port OMA monitoring circuit,” IEEE J. Solid-State Circuits **51**, 2328–2344 (2016).
16. T. Horikawa, D. Shimura, H. Okayama, *et al.*, “A 300-mm silicon photonics platform for large-scale device integration,” IEEE J. Sel. Top. Quantum. Electron. **24**, 8200415 (2018).
17. T. Horikawa, D. Shimura, H. Okayama, *et al.*, “Resonant wavelength variation modelling for microring resonators based on fabrication deviation analysis,” in *European Conference on Optical Communication (ECOC)* (2017), pp. 1–3.
18. P. Le Maître, J. F. Carpentier, C. Baudot, *et al.*, “Impact of process variability of active ring resonators in a 300 mm silicon photonic platform,” in *European Conference on Optical Communication (ECOC)* (2015), pp. 1–3.
19. D. Pérez-López, A. López, P. DasMahapatra, *et al.*, “Multipurpose self-configuration of programmable photonic circuits,” Nat. Commun. **11**, 6359 (2020).
20. W. Bogaerts, D. Pérez, J. Capmany, *et al.*, “Programmable photonic circuits,” Nature **586**, 207–216 (2020).
21. H. Yu, D. Korn, M. Pantouvaki, *et al.*, “Using carrier-depletion silicon modulators for optical power monitoring,” Opt. Lett. **37**, 4681–4683 (2012).
22. K. Goi, N. Ishikura, H. Ishihara, *et al.*, “Low-voltage silicon Mach-Zehnder modulator operating at high temperatures without thermoelectric cooling,” in *Optical Fiber Communications Conference and Exhibition (OFC)* (2015), pp. 1–3.
23. H. Zhu, K. Goi, and K. Ogawa, “All-silicon waveguide photodetection for low-bias power monitoring and 20-km 28-Gb/s NRZ-OOK signal transmission,” IEEE J. Sel. Top. Quantum. Electron. **24**, 4400207 (2018).
24. X. Xiao, X. Li, H. Xu, *et al.*, “44-Gb/s silicon microring modulators based on zigzag PN junctions,” IEEE Photonics Technol. Lett. **24**, 1712–1714 (2012).
25. X. Li, Z. Li, X. Xiao, *et al.*, “40 Gb/s all-silicon photodetector based on microring resonators,” IEEE Photonics Technol. Lett. **27**, 729–732 (2015).
26. J. B. You, H. Kwon, J. Kim, *et al.*, “Photon-assisted tunneling for sub-bandgap light detection in silicon PN-doped waveguides,” Opt. Express **25**, 4284–4297 (2017).
27. Y. Yuan, W. V. Sorin, D. Liang, *et al.*, “Mechanisms of enhanced sub-bandgap absorption in high-speed all-silicon avalanche photodiodes,” Photonics Res. **11**, 337–346 (2023).
28. Y. Yuan, W. V. Sorin, Z. Huang, *et al.*, “A 100 Gb/s PAM4 two-segment silicon microring resonator modulator using a standard foundry process,” ACS Photonics **9**, 1165–1171 (2022).
29. X. Xiao, L. Wang, J. Liu, *et al.*, “Silicon microring-based modulators and photodetectors beyond 100 Gbaud,” in *27th OptoElectronics and Communications Conference (OECC) and 2022 International Conference on Photonics in Switching and Computing (PSC)* (2022), pp. 1–3.
30. Y. Zhang, H. Zhang, J. Zhang, *et al.*, “240 Gb/s optical transmission based on an ultrafast silicon microring modulator,” Photonics Res. **10**, 1127–1133 (2022).
31. M. Sakib, P. Liao, C. Ma, *et al.*, “A high-speed micro-ring modulator for next generation energy-efficient optical networks beyond 100 Gbaud,” in *CLEO: Science and Innovations* (2021), paper SF1C-3.
32. Y. Yuan, Y. Peng, Z. Huang, *et al.*, “An O-band all-silicon microring avalanche photodiode with >38 GHz RF bandwidth,” in *IEEE Silicon Photonics Conference (SiPhotonics)* (2023), pp. 1–2.
33. R. Soref and B. Bennett, “Electrooptical effects in silicon,” IEEE J. Quantum Electron. **23**, 123–129 (1987).
34. V. Van, *Optical Microring Resonators: Theory, Techniques, and Applications* (CRC Press, 2016).
35. S. S. Li, *Semiconductor Physical Electronics* (Springer, 2012).
36. M. J. Lee, H. Rücker, and W. Y. Choi, “Optical-power dependence of gain, noise, and bandwidth characteristics for 850-nm CMOS silicon avalanche photodetectors,” IEEE J. Sel. Top. Quantum Electron. **20**, 211–217 (2014).
37. J. F. Buckwalter, X. Zheng, G. Li, *et al.*, “A monolithic 25-Gb/s transceiver with photonic ring modulators and Ge detectors in a 130-nm CMOSSOI process,” IEEE J. Solid-State Circuits **47**, 1309–1322 (2012).
38. D. Guermandi, L. Bogaerts, M. Rakowski, *et al.*, “TSV-assisted hybrid FinFET CMOS — silicon photonics technology for high density optical I/O,” in *45th European Conference on Optical Communication (ECOC)* (2019), pp. 1–4.
39. M. Raj, Y. Frans, P. C. Chiang, *et al.*, “Design of a 50-Gb/s hybrid integrated Si-photonic optical link in 16-nm FinFET,” IEEE J. Solid-State Circuits **55**, 1086–1095 (2020).
40. Y. Ban, M. Kim, P. De Heyn, *et al.*, “Highly optimized O-band Si ring modulators for low-power hybrid CMOS-SiPho transceivers,” in *Optical Fiber Communications Conference and Exhibition (OFC)* (2023), pp, 1–3.
41. https://www.cornerstone.sotonfab.co.uk/.
42. S.-H. Jeong, D. Shimura, T. Simoyama, *et al.*, “Si-nanowire-based multistage delayed Mach–Zehnder interferometer optical MUX/DeMUX fabricated by an ArF-immersion lithography process on a 300 mm SOI wafer,” Opt. Lett. **39**, 3702–3705 (2014).
43. Z. Mohammed, B. Paredes, and M. Rasras, “CMOS compatible ultracompact MMI based wavelength diplexer with 60 Gbit/s system demonstration,” Opt. Express **30**, 8257–8265 (2022).
44. https://doi.org/10.5258/SOTON/D2921.